

## Geometry of $(2 \times 2)\text{S}/\text{Cu}(001)$ determined with use of angle-resolved-photoemission extended fine structure

C. C. Bahr,\* J. J. Barton,<sup>†</sup> Z. Hussain,<sup>†</sup> S. W. Robey,<sup>†</sup> J. G. Tobin,<sup>§</sup> and D. A. Shirley  
*Materials and Molecular Research Division, Lawrence Berkeley Laboratory, University of California,  
 Berkeley, California 94720*

*and Department of Chemistry and Department of Physics, University of California, Berkeley, California 94720*

(Received 27 May 1986)

We have measured the adsorption geometry for the  $(2 \times 2)\text{S}/\text{Cu}(001)$  surface, including the reconstruction and relaxation of the copper substrate. Multiple-scattering spherical-wave calculations were compared with angle-resolved-photoemission extended-fine-structure data and these results were then compared with a Fourier analysis of the data. The sulfur atoms are located in the fourfold hollow site, with a S—Cu bond distance of 2.26(1) Å. With  $\frac{1}{4}$  monolayer “ $p(2 \times 2)$ ” sulfur coverage the symmetry of the copper substrate is necessarily lowered from  $(1 \times 1)$  to  $(2 \times 2)$ . Accordingly, the sulfur adsorption induces reconstruction and relaxation of the two topmost Cu layers. All the movement occurs in  $\text{Cu}_5\text{S}$  moieties, as if the surface were forming  $\text{Cu}_5\text{S}$  clusters embedded in the bulk. The first-layer Cu atoms are shifted  $\approx 0.06$  Å towards the third Cu layer and 0.05(2) Å laterally towards S. The second-layer Cu atoms under S atoms mimic the surface texture, in that they are 0.13 Å farther from the third layer than the bulk spacing would predict. Second-layer Cu atoms under fourfold open sites are close to positions predicted by the bulk spacing. Details of the data analysis and extraction of surface-structural parameters are presented.

### I. INTRODUCTION

The low-pressure adsorption of sulfur on the Cu(001) surface leads to three low-energy electron-diffraction (LEED) structures.<sup>1–5</sup> The first,  $(2 \times 2)$ , is thought to be a simple overlayer with sulfur in fourfold hollow sites of the unreconstructed substrate.<sup>1–3</sup> The  $(2 \times 2)$  structure is interesting as a precursor to higher-coverage states. The second pattern<sup>4</sup> is  $(2 \times 1)$ , which is a saturation coverage ( $\sim 0.5$  monolayers S) prepared at low  $\text{H}_2\text{S}$  dosing pressure ( $\sim 2 \times 10^{-9}$  Torr). The third structure<sup>1,5</sup> is also a saturation coverage (0.47 monolayers S), prepared by dosing at a higher pressure of  $\text{H}_2\text{S}$  ( $5 \times 10^{-6}$  Torr). The LEED pattern for the third structure has been modeled with two complicated adsorption domains.<sup>5</sup>

Preliminary work<sup>3</sup> on the  $(2 \times 2)$  structure located sulfur in the fourfold hollow,  $\sim 1.38$  Å above the top Cu plane. In this paper we report a more complete angle-resolved-photoemission extended-fine-structure (ARPEFS) study from which we have extracted additional structural information. This work will address not only the sulfur adsorption site, but also the positions of nearby copper atoms in the first and second layers. Because we know that the clean Cu(001) surface is essentially unreconstructed,<sup>6</sup> the relaxation and reconstruction of the surface are due entirely to the influence of sulfur.

This paper is divided into seven sections. Section II contains a brief review of the theoretical background of angle-resolved-photoemission extended-fine-structure. Section III contains a description of the experimental procedure used to prepare and measure the  $\text{S}(1s)$  ARPEFS. Section IV is a discussion of the data reduction from a series of photoelectron spectra to curves representing  $\chi(k)$ , the oscillating part of the photoelectron emission in-

tensity, as a function of electron wavelength,  $k$ . Section V discusses methods used to extract geometrical data for the ARPEFS curves. Section VI is a discussion of the error and reliability of the ARPEFS analysis. The final section summarizes our results for the  $(2 \times 2)\text{S}/\text{Cu}(001)$  data.

### II. THEORETICAL BACKGROUND

Barton and Shirley<sup>7–9</sup> have presented a complete description of the theory, which includes multiple-scattering, spherical-wave effects, correlated Debye-Waller factors, and analytic detector-aperture integration. Other workers offer similar theories.<sup>10</sup> We present here a brief review of the theoretical basis for ARPEFS.

This theory describes the changes in photoelectron intensity measured from an adsorbate atom as the exciting photon energy is changed. The changes in intensity are caused by interference among photoelectron waves which follow different paths from the emitter to the detector. One path is direct; the others involve one or more elastic scattering events off nearby atoms. Figure 1 shows the conventions used in describing the ionization and scattering. The origin is placed at the emitting atom. The polarization vector is labeled  $\hat{e}$  and the detector is located in the direction  $\mathbf{R}$ . Single scattering (one scattering center,  $\mathbf{a}$ ) and double scattering (depicted here as scattering from two centers,  $\mathbf{a}$  and  $\mathbf{b}$ ) account for most of the interference with the direct wave.

We can easily demonstrate a simple form for the interference pattern observed. First, we consider all possible paths from the emitter (at the origin,  $\mathbf{O}$ ) to the detector (at  $\mathbf{R}$ ). The direct photoelectron wave, or the photoionization in the absence of any scattering atoms, can be described in terms of Hankel functions and spherical har-

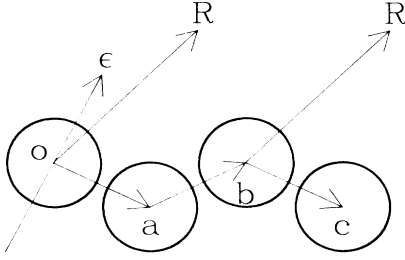


FIG. 1. Scattering geometry is defined. The emitting atom at the origin is labeled  $o$ . The detector lies in the direction  $\mathbf{R}$ . Shown here is a double scattering event, with a path from  $o$  to the intermediate atom  $a$ , and then from the atom  $b$  to the detector. Additional scattering atoms are labeled  $c, d$ , etc.

monics. Let us consider the simplest possible term:

$$\psi_0 \sim M(k) \frac{e^{ikR}}{kR}.$$

A single-scattered wave  $\psi_s$  based on this term is proportional to the product of the direct wave at the scattering atom  $\mathbf{a}$  and the scattering power  $|F|$ . The scattering factor  $F$  contains all the details of the scattering, such as the thermal averaging, angular aperture averaging, and scattering amplitude, to be discussed further in Sec. V. We form the proportional oscillations by normalizing to the atomic cross section. For a single-scattering atom at  $\mathbf{a}$ ,

$$\begin{aligned} \chi(k) &= \frac{I - I_0}{I_0} = \frac{(\psi_0 + \psi_s)^*(\psi_0 + \psi_s) - \psi_0^* \psi_0}{\psi_0^* \psi_0} \\ &= \frac{\psi_0^* \psi_s + \psi_s^* \psi_0 + \psi_s^* \psi_s}{\psi_0^* \psi_0} \\ &\approx \frac{|F|}{a} e^{-ikR} e^{ik|R-a| + i\phi} e^{ika} \\ &\quad + \frac{|F|}{a} e^{ikR} e^{-ik|R-a| - i\phi} e^{-ika} \\ &\quad + \left[ \frac{|F|}{a} \right]^2. \end{aligned} \quad (1)$$

Here,  $\phi$  is the phase of  $F$ , i.e.,  $F = |F| e^{i\phi}$ . We can also show that

$$\chi(k) \approx \frac{F}{a} \left[ 2 \operatorname{Re} \left( e^{ik(a-a \cos \theta_{aR}) + i\phi} \right) + \frac{F}{a} \right],$$

and

$$\chi(k) \approx \frac{2F}{a} \cos[k(a-a \cos \theta_{aR}) + \phi]. \quad (2)$$

Thus the scattering for a single atom would result in a cosine wave with a frequency  $(a-a \cos \theta)$  in the data  $\chi(k)$ . This formula suggests that Fourier transformation of the data would extract  $(a-a \cos \theta)$  directly, for scattering off a single atom. In a real lattice, multiple scattering and interference will complicate the Fourier transform.

### III. EXPERIMENTAL METHODS

In this experiment, a  $(2 \times 2)$  sulfur overlayer was prepared on a Cu(001) crystal and ARPEFS measurements were made in three different emission directions. The following is a description of the sample preparation and measurement.

A single crystal of Cu was cut, polished, and oriented to within  $0.5^\circ$  of the (001) plane. It was mounted on a manipulator, allowing three independent translations and two independent rotations in ultrahigh vacuum. The electron emission and photon polarization angles were calibrated using laser autocollimation referred to the sample surface. The rotation of the sample about the vertical axis and the azimuthal orientation of the sample about the sample normal are accurate to within  $2^\circ$ .

The clean Cu surface was prepared with standard techniques. It was bombarded with 1.5 keV  $\text{Ar}^+$  ions to remove surface contamination. The sputtering was alternated with a few heating cycles to 850 K to restore the surface crystallinity and to release bulk contaminants. The final annealing temperature of 500 K was chosen to minimize further diffusion of the bulk contaminants (S,C,O) to the surface. The LEED pattern observed from the clean surface was  $(1 \times 1)$  with a low background and sharp spots. The sulfur-covered surface was prepared by exposing the clean sample to 40 L [1 langmuir  $\text{L} \equiv 1 \times 10^{-6}$  Torr sec] of  $\text{H}_2\text{S}_{(g)}$  and flashing to 500 K to desorb H and improve the low-energy electron-diffraction pattern. The sulfur overlayer produced a  $(2 \times 2)$  LEED pattern, sometimes referred to as primitive, or  $p(2 \times 2)$ .

The ARPEFS measurement was performed at the Stanford Synchrotron Radiation Laboratory on the JUMBO beam line (III-3).<sup>11</sup> The monochromator provided photons through the energy range of this experiment,  $2500 \text{ eV} \leq h\nu \leq 3000 \text{ eV}$ . The Ge(111) monochromator crystals had a resolution of about 2 eV. The sample chamber and monochromator shared the ultrahigh vacuum of the storage ring. A thin carbon filter was inserted "upstream" of the monochromator to reduce the visible and vuv radiation, and as well as the heat load, on the first monochromator crystal. Photoelectron spectra were collected with a hemispherical angle-resolving spectrometer<sup>12</sup> mounted on a two-circle goniometer. The electron energy resolution was about 1 eV. We collected 100–130 photoelectron spectra, separated by 3–6 eV in photon energy, for each ARPEFS curve.

Our measurements are labeled [001], [011], and [111]. These correspond to the emission angles aligned with each of these three crystallographic directions. The [001] geometry is emission normal to the surface, with the photon polarization vector  $30^\circ$  from normal, towards the [010] axis. The [011] geometry has the polarization vector  $15^\circ$  from normal, towards the [011] direction. The [111] geometry was measured with the polarization vector tipped  $84.7^\circ$  from the normal, through [111]. The emission vectors are depicted in Fig. 2.

### IV. DATA REDUCTION

The objective of the data analysis is to convert a sequence of photoelectron spectra into proportional modula-

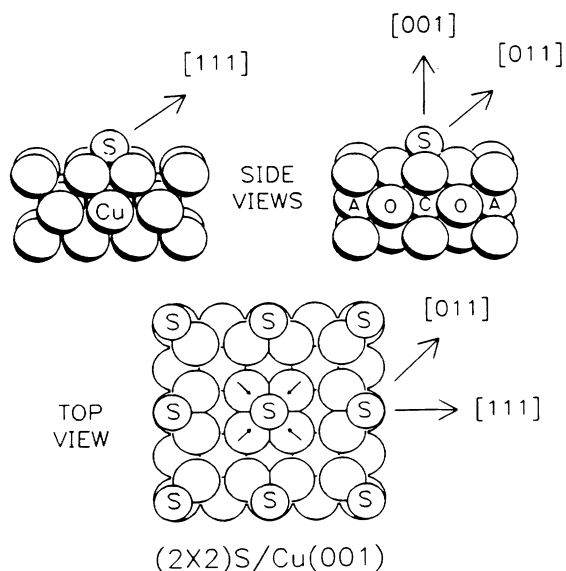


FIG. 2. Depiction of the measurement geometry. The emission angles are aligned with [001], [011], and [111]. The top view illustrates our model of the (2×2) sulfur overlayer. The side views are slices through the crystal along the [011] or [111] directions. The second-layer copper atoms are labeled C, O, or A for those covered by sulfur, those uncovered by sulfur in two-fold symmetric sites, and those uncovered in fourfold symmetric sites, respectively. The reconstruction of the top copper layer is shown exaggerated in the views.

tions,  $\chi(k)$ , of the photoelectron intensity. The S (1s) photoelectron peaks must be integrated (or fitted) and then multiplied with normalization factors relating them to a constant photon flux. Then the slowly varying part of the background is removed to form  $\chi(k)$ .

Initially we will define the photoelectron intensity in terms of the variable parameters for this experiment. We measure a spectrum:

$$N(E, h\nu, \mathbf{R}, \hat{\mathbf{e}}) = e(E) \{ F(h\nu) [ I(E, h\nu, \mathbf{R}, \hat{\mathbf{e}}) + B_F(E, h\nu, \mathbf{R}, \hat{\mathbf{e}}) ] + S(h\nu) B_S \} + D. \quad (3)$$

$N$  is the counting rate of electrons detected in the spectrometer as a function of the kinetic energy,  $E$ , the photon energy,  $h\nu$ , the sample to detector direction,  $\mathbf{R}$ , and the photon polarization vector,  $\hat{\mathbf{e}}$ . The index  $h\nu$  uniquely identifies each photoelectron spectrum.  $N$  is proportional to the incident monochromatic light flux  $F$  and the sum of the photoemission partial cross section  $I$  and the electron background cross section  $B_F$ .  $B_F$  is the electron background caused by (i) electrons which have suffered inelastic collisions in the solid before detection, (ii) full-energy Auger-electron transitions, and (iii) photoelectrons from the core level of interest, but at lower kinetic energy. There is an additional term,  $SB_S$ , which is the scattered polychromatic photon intensity multiplied by the cross section for producing any sort of electron background as a

result. The electron spectrometer efficiency  $e$  varies roughly as  $E^{-1}$  for our spectrometer.<sup>12</sup> Finally, the dark signal  $D$  is negligible for our experiments.

Equation (3) indicates the effects we must correct for in the conversion of photoelectron spectra into  $\chi(k)$ . It does not reflect the shape of each spectrum or the difficulty of extracting the photoelectron intensity. We apply Eq. (3) in a process of peak fitting [to isolate S (1s) electrons from background] and normalization (to correct for fluctuations in light intensity). Our structural analysis is quite insensitive to the selection of various peak-fitting and normalization algorithms.

### A. Curve fitting

Our first analysis step, curve fitting, is illustrated in Fig. 3. The spectrum has been deconvoluted into a Gaussian peak, a Gaussian-broadened step function, and a background function. We employed various minimization algorithms in our deconvolution. The simplicity of the fitting functions made the choice of *algorithms* arbitrary. The choice of *fitting functions* was dictated by two problems, energy-loss structure and Auger peak interference.

The energy-loss structure arises, in part, because core-level photoemission from metals has an asymmetric Doniach-Sunjić<sup>13</sup> line shape. The electrons contributing to the peak asymmetry (or the inelastic tail) have lost a small amount of energy by exciting conduction-band electrons. The question of whether to include or exclude the inelastic electrons depends on how the energy loss occurs. If the loss accompanies the primary photoemission event (intrinsic loss), then the electrons should be included.<sup>14</sup> On the other hand, if the loss occurs as an inelastic scattering event after photoemission (extrinsic loss), then these electrons will not be coherently related to their ini-

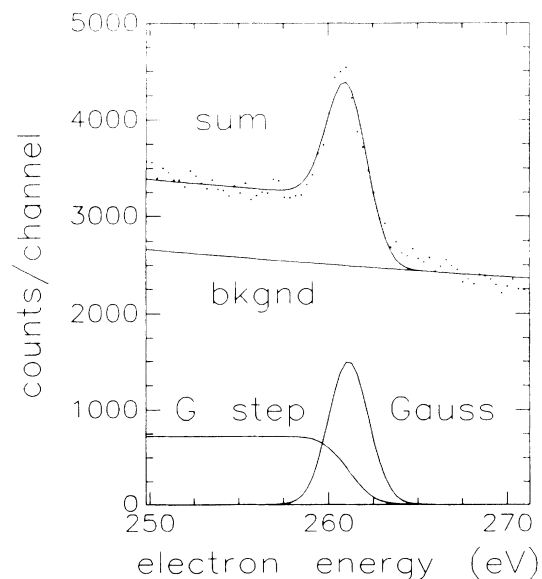


FIG. 3. Fitting functions are shown for a typical S(1s) electron spectrum. The dots are the data and lines are the fitting functions: Gaussian peak, Gaussian-broadened step, empirical background template, and their sum.

tial state, and hence will not contribute to the ARPEFS signal. Because we cannot separate the intrinsic and extrinsic contributions, we shall exclude the spectral intensity in the inelastic tail from the ARPEFS analysis.

The second complication of peak fitting is Auger-peak interference. Auger-peak intensities can be comparable to that of the photoelectron peak. Since the S LMM Auger peak is fixed in kinetic energy ( $\sim 150$  eV) and the S(1s) photoelectron peak is fixed in binding energy, there is a coincidence of peaks at  $h\nu \approx 2625$  eV, making curve fitting difficult. We reply on the generation of a precise background template which includes the Auger peaks so that our peak fitting will not fail in regions of coincidence. A perfect template would be the function  $FB_F + SB_S$  in Eq. (3). We spanned our ARPEFS energy range with four overlapping background templates. The photon energy was adjusted for each template so that the S(1s) peak was slightly lower in energy than the template energy range. We then formed a composite template spanning the entire ARPEFS energy range.

### B. Normalization

Our second analysis step is the construction of normalization factors relating photoelectron intensity from one spectrum to the next. This is crucial because the photon flux often varies by up to an order of magnitude during the course of an ARPEFS measurement. A photon flux monitor upstream of the ARPEFS apparatus does not always reflect the flux at the focal spot ( $< 1$  mm<sup>2</sup>) of the electron spectrometer. We have therefore used an internal reference. In terms of Eq. (3), the internal reference is  $FB_F + SB_S$ , or the background template. We expect the background to have a constant shape at different photon energies because much of the background is inelastically scattered electrons originating from many sources in the sample. These should not have a highly photon-energy-dependent cross section. We checked the dependence of the cross section on photon energy by determining another series of normalization factors. These new factors were computed by dividing overlapping portions of adjacent photoelectron spectra to form *relative* normalization factors. Our ARPEFS analysis was insensitive to the selection of different reasonable normalization factors.

### C. Removing $I_0$

Finally, we have constructed the functions  $I(E)$  as the Gaussian-peak areas multiplied by relative normalization factors. We now extract our proportional modulations,  $\chi(k)$ , by removing the atomiclike background  $I_0(E)$ . The cross section is known approximately but the measurement contains enough monotonic systematic errors (uncertain analyzer transmission, peak-fitting methods) that theoretical cross sections are not very useful. We extract a low-order polynomial from the  $I(E)$  to remove any low-frequency information or errors. The polynomial we used is  $A + BX + CX^2 + D/X + E/X^2$ . Cubic splines gave similar results. The  $I(E)$  is divided by  $I_0(E)$  and 1.0 is subtracted from the ratio [see Eq. (1)]. The absence of very low-frequency amplitude in the Fourier transform is the main background selection criterion. Figure 4 shows

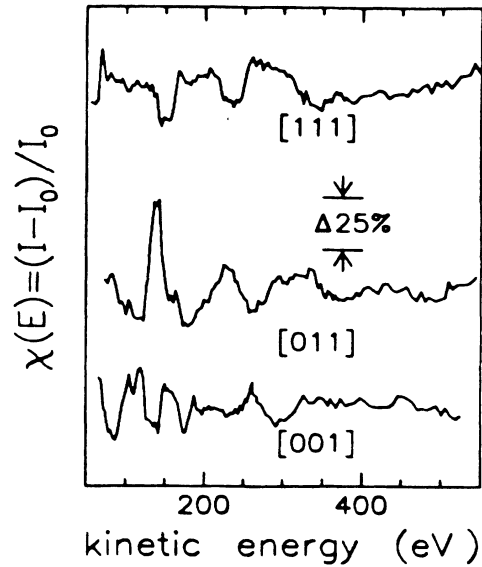


FIG. 4. Three  $\chi(E)$  curves are shown for measurements taken in the [001], [011], and [111] crystallographic directions relative to the Cu bulk. Each curve is the fractional modulation of the S(1s) intensity as a function of photon (or photoelectron) energy.

the  $\chi$  curves as functions of photoelectron kinetic energy. The curves are plotted on the same vertical scale.

## V. GEOMETRICAL ANALYSIS

The objective of the geometrical analysis is to determine the positions of the scattering atoms relative to the emitting atom. Figure 2 illustrates the local environment of sulfur. The low coverage ( $\sim \frac{1}{4}$  monolayer) of sulfur makes three types of second-layer copper atoms inequivalent: those covered by sulfur above, Cu(2c), those under fourfold symmetric empty sites (anti), Cu(2a), and those under twofold symmetric empty sites (open), Cu(2o). In this section we will address the local geometry of sulfur in reference to the positions of Cu(1), Cu(2a), Cu(2o), Cu(2c), and Cu(3). Two methods of analysis will be applied, direct Fourier analysis and multiple-scattering spherical-wave (MSSW) calculations. The methods of Barton *et al.*<sup>15</sup> were used as a guide in our MSSW analysis.

### A. Fourier analysis

The goal of the Fourier-transform analysis is to provide a "fingerprint" of the local geometry, and, where appropriate, to extract simple geometrical parameters. The advantages of direct Fourier analysis are that it is easy to implement, it is computationally efficient, and it requires minimal theoretical input. However, subtle effects such as surface relaxation and reconstruction usually cannot be derived from Fourier analysis. The transform process requires three steps: (i) converting from an energy to momentum scale, (ii) windowing (weighting) and extrapolating, and (iii) Fourier transforming.

In our first step we convert  $E$  to  $k$  using the de Broglie relation  $(E + E_0) = \hbar^2 k^2 / 2m$ . The energy  $E$  is measured relative to the vacuum level, so it must be related to the energy inside the crystal by adding the inner potential  $E_0$ . We then form the momentum as  $k = (1/\hbar)[2m(E + E_0)]^{1/2}$ .

The second step, windowing, is required because  $\chi(k)$  is not an infinite sequence of sine waves. Instead, the data have been truncated into a finite measurement range. Also, the sinusoidal functions have complicated phase shifts and amplitudes, as described in Eq. (2). The sharp truncation of the data has two effects: The finite data range limits our ability to resolve similar scattering path lengths and the abrupt onset of the data introduces oscillations in the Fourier coefficients. We extend the data range artificially using autoregressive (AR) extrapolation.<sup>16</sup> The AR method prohibits strong amplitude variations over  $k$ , so we arbitrarily multiply our data by  $k^2$  prior to AR extrapolation. After AR extrapolation we taper the new end points of the data by applying a Gaussian window (area = 1.0, mean = 8.5 Å<sup>-1</sup>, full width at half maximum (FWHM) = 7 Å<sup>-1</sup>). The modified  $\chi(k)$  rises smoothly from zero and appears uniform in amplitude over the actual measured region.

In our third step we apply the fast-Fourier-transform (FFT) algorithm<sup>17</sup> to form a Fourier power spectrum in path-length difference space. The Hilbert inverse transform<sup>18</sup> of a portion of the Fourier spectrum is formed, which represents the phase and amplitude of that portion, but in  $k$  space. The total phase,

$$\Phi(k) = kr(1 - \cos\theta) + \phi(k),$$

is obtained for a single peak in the  $r$ -space data. If contributions to the Fourier peak are dominated by a single scattering atom, then the peak can be back-transformed and the scattering phase shift  $\phi(k)$  removed to give the path-length difference  $r(1 - \cos\theta)$  directly, with an accuracy dependent on uncertainties in the nonstructural parameters, the extent to which other scatterers contribute, etc.

Fourier transforms of  $\chi(k)$  for the [001], [011], and [111] data are shown in Fig. 5. These spectra constitute an excellent diagnostic device for establishing the local site symmetry as a fourfold site, with the sulfur atom situated  $\sim 3.3$  Å above a second-layer copper atom, Cu(2c), and  $\sim 2.2$  Å from each of four nearest-neighbor copper atoms in the surface layer, Cu(1). These conclusions can be drawn by simple inspection of the Fourier-peak positions, or by Fourier back-transform analysis. The assignment of the origins of the Fourier peaks and subsequent extraction of structural data are useful exercises in verifying our structural model, but we will limit our discussion to four peaks. The 4.4-Å peak in the [011] transform is caused mostly by backscattering at 172° off the near-neighbor Cu(1) atom "opposite" sulfur from the detector. The 6.6-Å [011] peak is dominated by backscattering off the Cu(2c) atom directly below S, but contributions from higher path-length scattering atoms complicate the Fourier analysis. An interesting phenomenon is exhibited by two peaks at 3 and 4.5 Å in the [001] transform. These peaks arise from a single scattering path-length

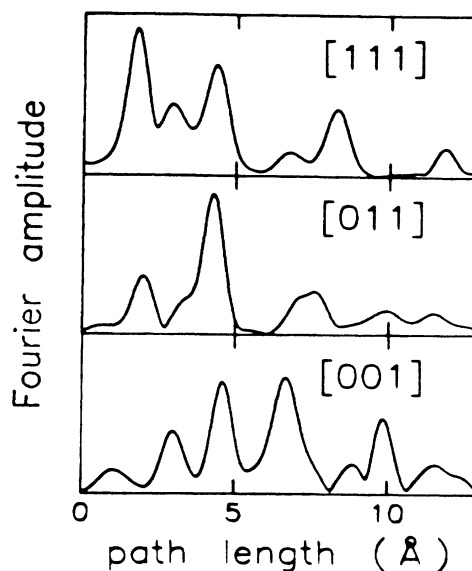


FIG. 5. Fourier amplitudes for the three data sets are shown here. The specific origins of several peaks are described in the text. In general, peaks represent scattering atoms at positions  $r(1 - \cos\theta)$ , with the bond distance  $r$  and the scattering angle  $\theta$ .

difference: scattering from the four (equivalent) nearest-neighbor atoms. The generalized Ramsauer-Townsend effect<sup>19</sup> causes the peak splitting by introducing a sudden phase change in a particular energy in the scattering amplitude at certain angles, 130° in this case. This effect was also observed for  $c(2 \times 2)$ S/Ni(001).<sup>20</sup>

We have used the standard back-transform method<sup>18</sup> to get a more accurate path-length difference for the 4.4-Å, [011] peak. We used the multiple-scattering spherical-wave theory described in Secs. II and VB to calculate the scattering phase shift for this peak. We also back-transformed the 6.6-Å, [001] peak, but the derived path-length difference is affected by additional scattering events contributing to the peak. The back-transform analysis results give path-length differences of 6.40(3) Å for [001] and 4.47(3) Å for [011]. We estimated these uncertainties by inspecting the variation of the back-transformed function  $r(1 - \cos\theta)$ , in each case, as a function of  $k$ . Assuming normal bulk-equivalent positions for the copper surface layer, these path-length differences would predict a 2.24-Å S—Cu(1) bond distance, a S—Cu(1)<sub>z</sub> separation of 1.33 Å, and a Cu(1)—Cu(2) separation of 1.87 Å, which would be 0.06 Å greater than the bulk value. In fact, the Cu(1)—Cu(2) separation is actually less than the bulk value, as the MSSW analysis given below will show. This comparison vividly illustrates the quantitative limitations of ARPEFS data analysis by Fourier methods. To anticipate the MSSW results, we will find that the Fourier back-transform analysis yields good agreement for the [001] 4.4-Å peak (i.e., a 0.02-Å discrepancy), but not for the [001] 6.6-Å peak (a discrepancy of 0.16 Å).

### B. Multiple-scattering spherical-wave theory

The MSSW calculations provide a basis for determining the positions of all atoms near the emitter. The comparisons of MSSW calculations to data probe the three-dimensional structure of the surface, and are not limited to a simple representation of atoms in path-length difference space, as are the Fourier transforms. We will describe the parameters required for the calculations and our approach to attaining a convergence on structural parameters.

Our scattering program takes as input the crystal structure, cluster size, emission and polarization angles, detector-aperture size, Debye temperatures, and scattering partial-wave phase shifts.

The sample is modeled with several infinite planes. Each plane is made of atoms with an origin  $(x, y, z)$  and two-dimensional unit vectors which allow any atomic position to be calculated. The atomic coordinates can be shifted to simulate surface relaxation and reconstruction. The cluster size is selected indirectly. We choose a threshold scattering amplitude which is required by the scattering program to select which atoms will be included in the cluster. Our program calculates the scattering amplitude for each atom successively in a spiral outward from the origin of each plane. When an entire spiral loop fails to meet the threshold, the program moves on to the next layer. First-, second-, third-, and fourth-order scattering have separate thresholds, so different orders of scattering can be turned on and off independently in the computation.

The emission and polarization angles are specified as polar and azimuthal angles relative to the sample  $z$  axis. The emission angle is treated as a variable parameter during the fitting of theory to data. The theory was analytically integrated over a detector aperture of  $\pm 3^\circ$ .

The Debye temperatures were chosen as in Ref. 15. The Cu bulk and surface  $z$ -axis Debye temperatures were 343 and 239 K, respectively. The  $z$ -axis S Debye temperature of 337 K was selected by giving it the same mean-squared displacement as the top layer Cu and then correcting for the mass difference. Our partial-wave phase shifts are from Orders and Fadley.<sup>21</sup> They were generated from a muffin-tin potential.

We now describe our procedure for determining a surface structure iteratively from calculations and data. Initially we calculated ARPEFS for several hypothetical geometries, the atop, bridge, and fourfold-hollow sites for S/Cu. The data and calculations for the [001], [011], and [111] experiments are shown in Figs. 6, 7, and 8, respectively. These test geometries assumed a 2.28-Å S—Cu bond distance obtained from the preliminary ARPEFS work<sup>3</sup> and unrelaxed bulk structural parameters. The fourfold site is clearly in the best agreement with experiment, although large differences between theory and experiment are still evident in the nonoptimized trial geometries.

After selecting the fourfold hollow site we began a global minimization of the weighted rms error  $\chi^2$  between the data and calculations. Since the simple  $\chi^2$  is sensitive to low-frequency oscillations in the data or theory, we re-

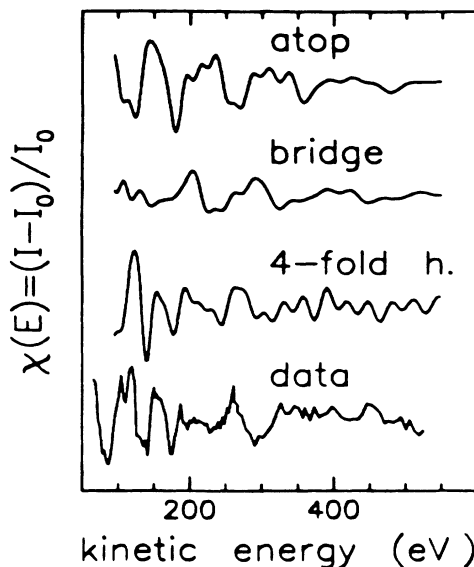


FIG. 6. Comparison of scattering calculations for three possible geometries: atop, bridge, and fourfold hollow, for the S/Cu adsorption. The data most closely resemble the fourfold-hollow calculation. These curves are for the [001] emission geometry.

moved these oscillations by removing a polynomial  $I_0$  from data and theory as in Eq. (1). We then minimized  $\chi^2$  by adjusting the following parameters: the emission angle, S-Cu(1)<sub>z</sub>, Cu(1)<sub>xy</sub> (lateral translation of Cu relative to sulfur), S-Cu(2a)<sub>z</sub>, S-Cu(2c)<sub>z</sub>, and S-Cu(3)<sub>z</sub>. Because the allowable parameter space was very large, we reduced the complexity of the calculations in several ways while searching for global minima. We reduced the maximum path-length difference for the calculation (reduced the size of the cluster), restricted the number of terms in

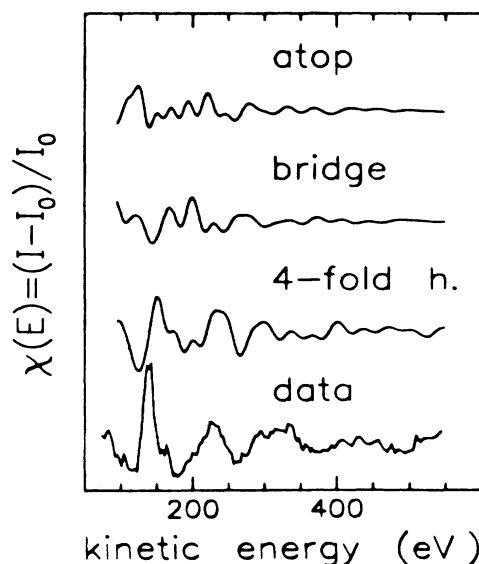


FIG. 7. Curves are calculated as in Fig. 5, but for the [011] emission geometry.

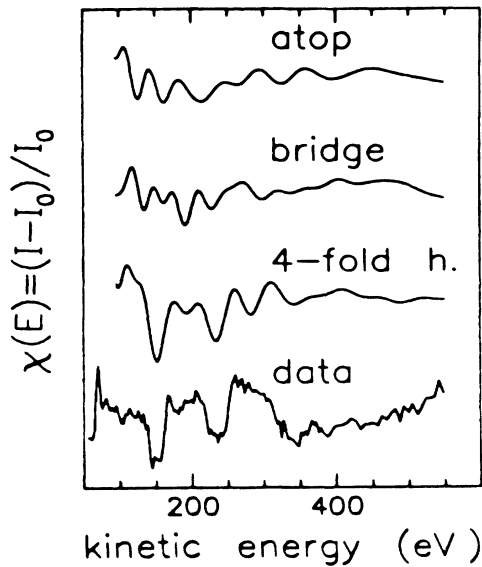


FIG. 8. Curves shown are calculated as in Fig. 5, but for the [111] emission geometry.

the spherical-wave approximation, and lowered the multiple-scattering order. Finally, we reoptimized the geometry around the minima with “full” calculations. The structural parameters derived from these calculations are listed in Table I.

The first adjustable parameter was the emission angle. Normal emission ARPEFS curves are usually fairly insensitive to the emission angle, and the [001] calculation did not change significantly with changes in this angle. The [011] and [111] calculations were very sensitive to the emission angles, however. No reasonable structural parameters could be found until their associated emission angles were changed. The optimum angle for [011] was 42° from normal (instead of the nominal 45°), but the op-

timum azimuth was unchanged. The optimum angle for [111] was 55.6° (instead of the nominal 54.7°), again with an unchanged azimuth. It is evident that better control of this parameter would reduce the experimental uncertainty in the future.

The first two structural parameters, S-Cu(1)<sub>z</sub> and Cu(1)<sub>xy</sub>, are closely coupled. Together they define the S—Cu bond length, which we determine to be 2.26(1) Å. The [001] calculations were optimized with a S-Cu(1) distance of 1.38 Å and a Cu(1)<sub>xy</sub> translation of 0.02 Å (0.00=bulk). The Cu—S—Cu bond angle inferred from these values is 104.7°. The [011] calculations were optimized with a S-Cu(1)<sub>z</sub> distance of 1.41 Å and a Cu(1)<sub>xy</sub> translation of 0.06 Å [inferred ∠(Cu—S—Cu)=102.3°]. The [111] calculations were optimized with a S-Cu(1)<sub>z</sub> distance of 1.44 Å and a Cu(1)<sub>xy</sub> translation of 0.04 Å [inferred ∠(Cu—S—Cu)=101.7°]. The agreement among these values is satisfactory, especially considering that the [001] values are both less precise and subject to uncertainties due to the generalized Ramsauer-Townsend effect.

The next three structural parameters were the distances from the sulfur plane to the covered, open, and anticovered second-layer copper atoms, or S-Cu(2c)<sub>z</sub>, S-Cu(2o)<sub>z</sub>, and S-Cu(2a)<sub>z</sub>, respectively. The parameters determined from the optimizations were in fair agreement among the different emission directions, with the general trend that the covered copper atoms were closer to the surface than the anticovered copper atoms. If we combine the average S-Cu(1)<sub>z</sub> values with the average S-Cu(2) values we can infer that the Cu(1)-Cu(2a) spacing is ~0.1 Å smaller than the bulk value of 1.81 Å and that the Cu(1)-Cu(2c) value is ~0.2 Å smaller than the bulk value. The Cu(1)-Cu(2o) spacing is intermediate, ~0.15 Å smaller than the bulk spacing.

The final structural parameter we optimized was the distance from sulfur to the third layer of copper. There is considerable scatter (±0.1 Å) in the results for S-Cu(3)<sub>z</sub>, which is to be expected, considering the great distance

TABLE I. Structural parameters (in angstroms) determined for (2×2)S/Cu(001), with uncertainties in parentheses. Multiple-scattering spherical-wave (MSSW) calculations were optimized to agree with the data by varying the positions of Cu atoms near the S emitter. Standard Fourier analysis has also been applied to derive simple parameters.

	[001] <sup>a</sup> FFT	[011] <sup>a</sup> FFT	[001] <sup>b</sup> MSSW	[011] <sup>b</sup> MSSW	[111] <sup>b</sup> MSSW	Avg. <sup>c</sup> MSSW
ΔCu(1) <sub>xy</sub>			-0.02(3)	-0.06(1)	-0.04(1)	-0.05(2)
S-Cu(1) <sub>z</sub>			1.38(2)	1.41(1)	1.44(1)	1.42(2)
S-Cu(2c) <sub>z</sub>	3.20(3)		3.06(3)	3.00(6)	3.03(2)	3.04(2)
S-Cu(2o) <sub>z</sub>			3.13(4)	3.16(4)	3.03(2)	3.07(6)
S-Cu(2a) <sub>z</sub>			3.16(2)	3.25(8)	3.14(4)	3.16(5)
S-Cu(3) <sub>z</sub>			4.88(4)	5.06(4)	4.96(4)	4.97(6)
S-Cu		2.24(3)	2.26	2.25	2.28	2.26(1)
∠(Cu—S—Cu)			104.7°	102.3°	101.7°	102.2(1.3)°

<sup>a</sup>Back-transform analysis of Fourier peaks described in the text. Uncertainties represent the deviation of the back-transformed path-length difference as a function of *k*.

<sup>b</sup>Least-squares analysis of data and MSSW calculations. Uncertainties are the standard deviations of the values estimated from the fit.

<sup>c</sup>“Average” geometry, determined from an error-weighted average of the MSSW results. Uncertainties are the rms deviations of the individual parameter values from the averaged values.

from sulfur to the third copper layer ( $\sim 5 \text{ \AA}$ ). The average value of  $S\text{-Cu}(3)_z$ , 4.97  $\text{\AA}$ , together with the  $S\text{-Cu}(2)_z$  values, can be used to infer the  $\text{Cu}(2)\text{-Cu}(3)$  spacing. The  $\text{Cu}(2c)\text{-Cu}(3)$  spacing appears to be expanded from the bulk value by  $\sim 0.1 \text{ \AA}$ , while the average  $\text{Cu}(2a)\text{-Cu}(3)$  spacing appears to model the bulk to within 0.01  $\text{\AA}$ .

Our structural analysis thus concludes that the second Cu layer moves slightly up from the bulk and the top Cu layer moves down towards the bulk, producing a much smaller measured  $\text{Cu}(1)\text{-Cu}(2)$  spacing (1.62  $\text{\AA}$ ) than the  $\text{Cu}(2)\text{-Cu}(3)$  spacing (1.93  $\text{\AA}$ ). The second layer is apparently reconstructed (buckled), with the  $\text{Cu}(2a)$  atoms 0.13  $\text{\AA}$  farther from the surface than the  $\text{Cu}(2c)$  atoms. The top layer copper atoms are translated  $\sim 0.05 \text{ \AA}$  laterally towards the sulfur adsorption site.

The calculated  $\chi(k)$  curves corresponding to the optimized geometries are shown in Fig. 9. The curves represent the best agreement between data and theory for all allowable parameter values. However, we can see by inspection that the remaining discrepancies between the calculations and data are greater than the statistical uncertainty of the data. Without additional, independent ARPEFS measurements, we cannot distinguish between systematic data collection errors and systematic errors in the theoretical calculations. For instance, the sulfur *LMM* Auger peak usually has some effect on the measured  $\chi(k)$  curves near 150 eV. Conversely, systematic errors in the calculations such as errors in the assumed structure or improper treatment of the scattering problem may introduce visible deviations of the calculated curves.

On the whole, the amount and consistency of structural information obtained from the MSSW fits are surprisingly good, even though the agreement between the curves and experiment, shown in Fig. 9, is far from perfect. We have eschewed trying to extract further structural information because our analysis was already somewhat overwhelmed

with adjustable structural parameters, listed in Table I. In planning the experiment we were unaware of the importance of, or the sensitivity of the  $\chi(k)$  curves to such subtle adjustments as the lateral displacements in the first-layer copper atoms. Based on our results (Table I), it seems probable that—given a large data set and a powerful multiparameter fitting routine—the ARPEFS method may be capable of yielding a fairly large set of surface structural parameters with good accuracy.

### C. Comparison of Fourier transform and MSSW

The Fourier analysis can yield ambiguous results because it provides only path-length differences. For example, the 4.4- $\text{\AA}$  peak in the [011] transform has a back-transformed path-length difference of 4.47  $\text{\AA}$ . If the origin of this peak is almost entirely a single copper atom, this path-length difference can be interpreted as yielding  $d_{S\text{-Cu}(1)_z} = 1.33 \text{ \AA}$  if the  $\text{Cu}(1)$  reconstruction is neglected and  $d_{S\text{-Cu}(1)_z} = 1.40 \text{ \AA}$  if 0.05- $\text{\AA}$  lateral reconstruction is included. Without a full MSSW analysis, this ambiguity would be unresolved. In either case, however, the S—Cu bond distance itself agrees well with the full analysis.

The  $S\text{-Cu}(2)_z$  value predicted from the [001] transform (3.20  $\text{\AA}$ ) is in poor agreement with the MSSW results [ $d_{S\text{-Cu}(2c)} = 3.04 \text{ \AA}$ ]. The Fourier-transform analysis cannot achieve high ( $\pm 0.05 \text{ \AA}$ ) accuracy results unless specific scattering path lengths can be resolved from other path lengths of comparable scattering amplitude.

In general, Fourier analysis can give a semiquantitative view of the path-length difference distribution of scattering atoms. This provides a powerful tool for screening proposed structures. However, complete, accurate structural determinations are not generally feasible from Fourier analysis. We cannot determine from the Fourier transform alone which of the Fourier peaks has enough contributions from inequivalent scattering atoms to invalidate a derived path-length difference. The comparison of theory to data in the  $k$  domain is less ambiguous than Fourier analysis, and it provides a more stringent test of a geometrical model.

## VI. ERROR ANALYSIS

An error analysis is crucial to the evaluation of the structural results. The error falls under two categories, precision and accuracy.

### A. Precision

The precision can be estimated statistically. Our approach is to consider the calculated curve,  $\chi(k)_{\text{theoretical}} = YC_i$ , as a function in  $k$  having several parameters  $P_j$ . These parameters are the geometrical values we wish to extract from the data. If we compare the data,  $\chi(k)_{\text{experimental}} = Y_i$ , with  $YC_i$  in a least-squares sense, we can estimate a  $\chi^2$  error:

$$\chi^2 = \sum_i [\sigma_i^{-2} (Y_i - YC_i)^2],$$

where  $\sigma_i$  is the standard deviation of a data point  $Y_i$ . The reduced  $\chi^2$  is then given by

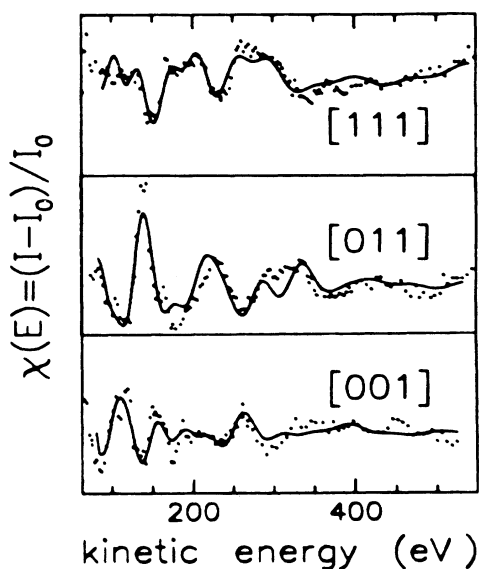


FIG. 9. Final optimized calculations are shown for each measurement direction. The data are shown as dots.

$$\chi_R^2 = \frac{\chi^2}{N-k-1},$$

where  $N$  is the number of data points,  $k$  is the number of adjustable parameters, and  $N-k-1$  is the number of degrees of freedom of the fit. Since the structural optimization is essentially a problem in nonlinear least-squares curve fitting, we can apply the results of Bevington.<sup>22</sup> Assuming that the adjustable parameters are independent and  $\chi_R^2 \approx 1$ , the standard deviation of a parameter is given by

$$\sigma_{P_j}^2 = \frac{2}{\partial^2 \chi^2 / \partial P_j^2}.$$

If, in fact,  $\chi_R^2 > 1$ , then we can approximately account for the poor fit by multiplying  $\sigma_{P_j}^2$  with  $\chi_R^2$  to form a more reasonable estimate of the standard deviation.

The precision of a parameter is thus determined statistically from three factors: the data precision, the goodness of fit, and the curvature of  $\chi^2$  in parameter space. The curvature of  $\chi^2$  is an inherent feature of the ARPEFS technique. We have listed the statistical uncertainties for the geometrical parameters determined from the MSSW analysis in Table I.

#### B. Accuracy

The accuracy depends mainly on the adequacy of the theoretical treatment of ARPEFS. Uncertain factors include the emission angle determination, the thermal correction (Debye-Waller), and the scattering potentials. The accuracy would be empirically estimated by comparing ARPEFS results to other techniques or by comparing several ARPEFS results obtained by varying the potentials or other factors within reasonable bounds. Our estimates are made by comparing independent ARPEFS results from the same sample. We will discuss contributions to inaccuracy here.

Our sample geometry is accurate to within 3°. It depends on the accuracy of preparing a crystal with a surface normal parallel to the crystalline axes. It also depends on the alignment of the crystal normal with the electron spectrometer and the incident photon beam. The effect of a 3° polar angle (rotation of the sample about the vertical axis) error can be estimated geometrically. The error depends on the angles chosen and the scattering event examined. For instance, backscattering (180° scattering angle) is insensitive to angular positioning errors. The error in a determined bond length would be

$$R_{OA}(\text{experimental}) = R_{OA}(\text{true})(1 - \cos 177^\circ) / (1 - \cos 180^\circ)$$

or about 0.1% too low. At a scattering angle of 125 degrees the error would be about 3%. Since we allow the emission angle to vary in our fits, the effect of this error may be reduced somewhat, but the uniqueness of the fit between data and theory is likewise reduced.

The remaining terms, thermal effects and scattering potentials, probably contribute less than 0.02 Å to the inaccuracy. Thermal effects mainly change the overall envelope of  $\chi$ . As pointed out by Barton,<sup>15</sup> the error introduced in an extended x-ray absorption fine-structure

(EXAFS) analysis by substituting Cu for Ni phase shifts is less than 0.02 Å.

Our estimate of the accuracy depends on which structural parameter we are extracting. The practical result from having multiple ARPEFS curves is that we can compare the parameter values extracted from the different curves. Nearly all the scatter in the values shown in Table I falls outside the expected range of statistical uncertainties. This means that, assuming experimental and theoretical systematic errors cancel when enough curves and emission directions are considered, the accuracy is given by the scatter in the parameter values. The structural values given in Table I indicate that our effective accuracy in determining an atomic position is  $\leq 3\%$  of the distance from the emitter to the scatterer. We also note that this accuracy is not usually limited by the precision of our data.

#### VII. CONCLUSIONS

We have measured and analyzed three independent ARPEFS curves for (2×2)S/Cu(001). We have applied two methods of analysis. The first, Fourier-transform analysis, has provided simple geometrical parameters easily. In fact, the preliminary Fourier analysis of S/Cu with plane-wave single-scattering phase shifts<sup>3</sup> determined a S—Cu bond length within 0.03 Å of the S—Cu bond distance determined in this work. The second method of analysis, employing MSSW calculations, has a much greater capability for yielding atomic positions. With our S/Cu data, we are able to observe surface relaxation and reconstruction.

The results of our MSSW optimizations are the following. The S—Cu bond distance is 2.26(1) Å. The sulfur adsorption induces a movement of the top Cu atoms 0.05(2) Å laterally towards the adsorption site and 0.06 Å towards the bulk. We have evidence for second-layer corrugation, with the copper atoms under fourfold sym-

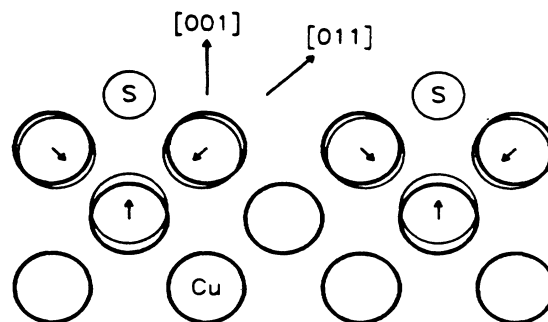


FIG. 10. Sulfur-induced reconstruction and relaxation of the copper surface are shown in a cross-sectional view along the [001] and [011] directions. The “covered” second-layer Cu atoms are shifted upwards and the “anticovered” second-layer Cu atoms have not moved. The out-of-plane second-layer Cu atoms, which are translated upwards less than the Cu(2c) atoms, are not shown in this figure. The top-layer Cu atoms are shifted downwards and laterally towards sulfur. The shifts in positions are exaggerated by a factor of 2.

metric open sites lying 0.13 Å lower than the copper atoms under sulfur. The distance from the sulfur emitter to the copper atom directly below is 3.04(2) Å. The effect of sulfur adsorption on the copper surface, estimated by comparing these ARPEFS results with previous LEED experiments on the clean Cu surface,<sup>6</sup> is illustrated in Fig. 10, where a cross section is taken through the [001] and [011] directions. Shifts in the positions of the Cu atoms near S are indicated with arrows.

Finally, ARPEFS is shown to be highly sensitive to the local three-dimensional environment of the emitting atom. ARPEFS provides a uniquely accurate tool for the determination of many surface structures. More theoretical work is needed to reduce inaccuracy to a level consistently below the experimental precision.

## ACKNOWLEDGMENTS

We thank P. J. Orders and C. S. Fadley for providing the partial-wave phase shifts of S and Cu. This work was supported by the Director, Office of Energy Research, Office of Basic Energy Sciences, Chemical Sciences Division of the U. S. Department of Energy under Contract No. DE-AC03-76SF00098. It was performed at the Stanford Synchrotron Radiation Laboratory, which is supported by the U. S. Department of Energy, Office of Basic Energy Sciences. Two of us (Z. H. and J. G. T.) acknowledge support by the University of Petroleum and Minerals under Project No. PHYS-ARPES-71 and by the National Science Foundation, respectively.

\*Present address: AT&T Engineering Research Center, P.O. Box 900, Princeton, NJ 08540.

†Present address: IBM Thomas J. Watson Research Center, P.O. Box 218, Yorktown Heights, NY 10598.

‡Present address: Department of Physics, University of Petroleum and Minerals, Dhahran 31261, Saudi Arabia.

§Present address: Department of Chemistry, University of Wisconsin—Madison, 1101 University Avenue, Madison, WI 53706.

<sup>1</sup>J. L. Domange, and J. Oudar, *Surf. Sci.* **11**, 124 (1968).

<sup>2</sup>J. R. Noonan, D. M. Zehner, and L. H. Jenkins, *Surf. Sci.* **69**, 731 (1977).

<sup>3</sup>J. J. Barton, C. C. Bahr, Z. Hussain, S. W. Robey, J. G. Tobin, L. E. Klebanoff, and D. A. Shirley, *Phys. Rev. Lett.* **51**, 272 (1983).

<sup>4</sup>R. W. Joyner, C. S. McKee, and M. W. Roberts, *Surf. Sci.* **27**, 279 (1971).

<sup>5</sup>V. Maurice, J. J. Legendre, and M. Huber, *Surf. Sci.* **129**, 312 (1983).

<sup>6</sup>D. L. Adams and U. Landman, *Phys. Rev. B* **15**, 3775 (1977); G. Kleiman and J. M. Burkstrand, *Surf. Sci.* **50**, 493 (1975).

<sup>7</sup>J. J. Barton and D. A. Shirley, *Phys. Rev. A* **32**, 1019 (1985).

<sup>8</sup>J. J. Barton and D. A. Shirley, *Phys. Rev. B* **32**, 1906 (1985).

<sup>9</sup>J. J. Barton and D. A. Shirley, *Phys. Rev. B* **32**, 1892 (1985).

<sup>10</sup>M. Sagurton, E. L. Bullock, R. Saiki, A. Kaduwela, C. R. Brundle, C. S. Fadley, and J. J. Rehr, *Phys. Rev. B* **33**, 2207 (1986).

<sup>11</sup>Z. Hussain, E. Umbach, D. A. Shirley, J. Stöhr, and J. Feldhaus, *Nucl. Instrum. Methods* **195**, 115 (1982).

<sup>12</sup>S. D. Kevan, Ph.D. thesis, University of California, Berkeley, 1980.

<sup>13</sup>S. Doniach and M. Šunjić, *J. Phys. C* **3**, 291 (1970).

<sup>14</sup>For instance, in an EXAFS measurement, photoelectron satellites (shake-up, shake-off, etc.) will give rise to their own EXAFS, shifted in photon energy from the main-line photoelectron. See, for example, K. D. Bomben, M. K. Bahl, J. K. Gimzewski, S. A. Chambers, and T. D. Thomas, *Phys. Rev. A* **20**, 2405 (1979); P. A. Lee and G. Beni, *Phys. Rev. B* **15**, 2862 (1977).

<sup>15</sup>J. J. Barton, C. C. Bahr, S. W. Robey, Z. Hussain, E. Umbach, and D. A. Shirley, *Phys. Rev. B* **15**, 3807 (1986).

<sup>16</sup>J. J. Barton and D. A. Shirley, Lawrence Berkeley Laboratory Report No. LBL-14758 (unpublished) and J. J. Barton, Ph.D. thesis, University of California, Berkeley, 1985, Chap. 6.

<sup>17</sup>E. O. Brigham, *The Fast Fourier Transform* (Prentice-Hall, Englewood Cliffs, N. J., 1974).

<sup>18</sup>G. Martens, P. Rabe, N. Schwentner, and A. Werner, *Phys. Rev. B* **17**, 1481 (1978).

<sup>19</sup>B. K. Teo and P. A. Lee, *J. Am. Chem. Soc.* **101**, 2815 (1979).

<sup>20</sup>J. J. Barton, C. C. Bahr, Z. Hussain, S. W. Robey, L. E. Klebanoff, and D. A. Shirley, in *Proceedings for the Brookhaven Conference, Advances in Soft X-ray Science and Technology* [SPIE J. **447**, 82 (1984)].

<sup>21</sup>P. J. Orders and C. S. Fadley, *Phys. Rev. B* **27**, 781 (1983), and private communication.

<sup>22</sup>P. R. Bevington, *Data Reduction and Error Analysis for the Physical Sciences* (McGraw-Hill, New York, 1969), Chap. 11.